

Interaction quench in the Holstein model: Thermalization crossover from electron- to phonon-dominated relaxation

Yuta Murakami,¹ Philipp Werner,² Naoto Tsuji,¹ and Hideo Aoki¹

¹*Department of Physics, The University of Tokyo, Hongo, Tokyo 113-0033, Japan*

²*Department of Physics, University of Fribourg, 1700 Fribourg, Switzerland*

(Dated: June 8, 2019)

We study the relaxation of an electron-phonon coupled system after a sudden switch-on of the interaction, and observe a qualitative change in the thermalization dynamics as the interaction is varied in the weak-coupling regime. This crossover is demonstrated for the Holstein model using the nonequilibrium dynamical mean-field theory with the self-consistent Migdal approximation as an impurity solver. For sufficiently weak interaction, phonon oscillations are damped rapidly compared to the electron thermalization timescale, as determined from the relaxation of the electron momentum distribution function. For sufficiently strong interaction, the relaxation of the electrons becomes faster than the phonon damping. In this regime, despite long-lived phonon oscillations, the electronic properties can be described by a thermal state with a time-dependent effective temperature. We trace back the origin of this “thermalization crossover” to distinct behaviors of the electron and phonon self-energies as a function of the electron-phonon coupling. In addition, the importance of the phonon dynamics is demonstrated by comparing the results from the self-consistent Migdal approximation to those obtained with a simpler Hatree-Fock impurity solver that neglects the phonon self-energy. The latter approximation cannot properly describe the evolution and thermalization of isolated electron-phonon systems.

PACS numbers: 71.38.-k, 71.10.Fd, 71.10.-w

I. INTRODUCTION

The nonequilibrium dynamics of strongly correlated lattice systems has recently been investigated intensively in various contexts.¹ Interaction-quench studies^{2–10} have been motivated by cold-atom experiments, where the interaction or hopping can be tuned by the Feshbach resonance or by changing the depth of the optical lattice potential. In condensed-matter experiments, on the other hand, one can drive correlated electron systems with strong lasers. These perturbations may induce phase transitions, e.g. from an insulating to a metallic state,^{11–14} and in some cases metastable phases with interesting properties.^{15,16} In real materials, the electron-phonon coupling can play a crucial role in the nonequilibrium dynamics, and indeed many pump-probe experiments exhibit clear signatures of phonon oscillations.^{12,17} From a theoretical point of view, the interplay of electronic and lattice degrees of freedom in out-of-equilibrium situations is still far from understood. Often, the experimental results are interpreted in terms of the phenomenological two-temperature model,¹⁸ which assumes that the electrons relax fast compared to typical phonon time scales, so that electrons can be assigned an effective temperature shortly after the perturbation.

Various techniques have been developed and used in recent years to study nonequilibrium electron-phonon systems on the microscopic level. In Ref. 19–21, the non-equilibrium dynamics of one or two polarons in the Holstein model was investigated with a time-dependent exact diagonalization method. Ref. 22, by solving a one-dimensional model coupled with classical phonons, discussed the relevance of different types of electron-phonon couplings for the transfer of energy to the lattice. Many electron problems in two-dimensional systems have been studied by an exact diagonalization method for

the Holstein-Hubbard model²³ and using weak-coupling perturbation theory for the Holstein model.^{24–26} In the framework of dynamical mean-field theory (DMFT),²⁷ which should be accurate in high dimensions, the interplay of electrons and phonons has been studied in the Mott insulating phase using a strong-coupling impurity solver.^{28,29} The latter simulations showed that the feedback of the lattice dynamics onto the electrons can lead to significant changes in the spectral function, and to qualitatively different relaxation pathways.

Despite this progress, studies treating the dynamics of quantum phonons are so far limited to systems in or near the Mott insulating phase.^{23,28,29} It thus remains to be clarified how an electron-phonon system thermalizes in weakly or moderately correlated metallic systems and how the phonon dynamics affects this relaxation process. In addition, various interesting questions that have been addressed in purely electronic systems (such as the Hubbard model) remain to be answered. For example, one may ask if the so-called prethermalization phenomena^{4,5,7,30} and dynamical phase transitions^{5,7,9,31,32} also occur in electron-phonon systems. Obtaining insights into the effects of the phonon dynamics is also important for establishing suitable approximate treatments and their limitations.

To address the above issues, we focus in this paper on the simplest possible model for an electron-phonon system, i.e., the Holstein model, which contains the coupling to local phonons but has neither Coulomb interactions nor a coupling to some phenomenological heat bath. By considering such a simple model, we hope to gain some fundamental insights into the generic relaxation and thermalization processes of electron-phonon system. We also consider the simplest possible kind of perturbation, i.e., to drive the system out of equilibrium by a sudden quench of the electron-phonon coupling. Such a situation may be realized in cold-atom systems on optical lattices.^{33–36}

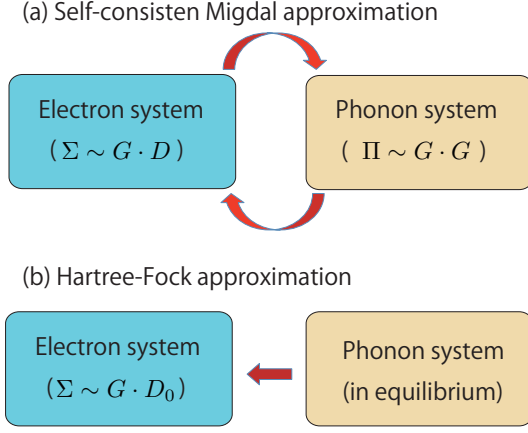


FIG. 1: The self-consistent Migdal approximation (a) and the Hartree-Fock approximation (b) are schematically depicted. G denotes the dressed electron Green's function and D the dressed phonon Green's function, while D_0 is the bare (equilibrium) phonon propagator. Σ and Π are the electron and phonon self-energies, respectively.

The model is solved using the nonequilibrium extension of DMFT.^{1,37} As an impurity solver for DMFT, we employ the Migdal approximation, which neglects the vertex correction in the self-energy and is based on the assumption that the phonon frequency and the electron-phonon coupling are small enough. This type of approximation has been successfully used to describe conventional superconductors in the strong-coupling regime, and has also been justified with numerical studies based on the DMFT framework.³⁸

We should note here that the term ‘‘Migdal approximation’’ is used for two different types of approximations in the literature on the Holstein model: One is the unrenormalized Migdal approximation,³⁹ where the *noninteracting* phonon propagator is used to express the effective interaction among the electrons. In other words, this approximation *does not* consider the phonon dynamics. This type of approximation has also been employed in recent studies of the dynamics of the Holstein model driven by strong laser fields.^{24–26} The other is the self-consistent Migdal approximation,^{38,40–44} where the *dressed* phonon propagator is used and thus the phonon dynamics affects the electron self-energy. In the following, we call the former approximation the Hartree-Fock (HF) approximation and the latter the Migdal approximation, see Fig. 1. We show that the Migdal approximation is more reliable than HF, by benchmarking equilibrium results against DMFT data obtained with a continuous-time quantum Monte Carlo (CT-QMC) impurity solver.⁴⁵ Then we use the Migdal approximation to discuss the dynamics of the isolated Holstein model after a sudden switch-on of the electron-phonon coupling.

The main finding of this study is that there exist two regimes of different relaxation processes depending on the electron-phonon coupling strength: for a weak electron-phonon coupling, the phonon oscillations are damped faster than the thermalization time of the electrons, while in a sufficiently strongly interacting system the relaxation of the phonons becomes slower than the electron relaxation. We furthermore show, by comparing the relax-

ation dynamics in the Migdal and HF approximations, that the explicit treatment of the phonon dynamics (i.e. the phonon self-energy) leads to qualitative changes in the relaxation dynamics.

This paper is organized as follows. In Sec. II, we introduce the Holstein model and discuss the nonequilibrium DMFT formalism for this model, as well as the Migdal and HF impurity solvers. We also discuss several properties of the phonon propagator in the Kadanoff-Baym formalism. In Sec. III, we first test the reliability of the HF and Migdal approximations in equilibrium. Then we explore the dynamics of the Holstein model after an interaction quench from the noninteracting state at zero temperature. We consider both the Migdal and HF impurity solvers to discuss their suitability for describing electron-phonon systems. In Sec. IV, we provide a conclusion and outlook.

II. MODEL AND FORMALISM

A. Nonequilibrium DMFT for the Holstein model

The Hamiltonian for the Holstein model is

$$\mathcal{H}(t) = -v \sum_{\langle i,j \rangle, \sigma} (c_{i,\sigma}^\dagger c_{j,\sigma} + \text{h.c.}) - \mu \sum_i n_i + \omega_0 \sum_i a_i^\dagger a_i + g(t) \sum_i (a_i^\dagger + a_i)(n_{i,\uparrow} + n_{i,\downarrow} - \alpha), \quad (1)$$

where $c_{i,\sigma}^\dagger$ is the creation operator for electrons with spin σ on site i , v is the hopping parameter, a_i^\dagger is the creation operator of phonons with frequency ω_0 , $g(t)$ is the (time-dependent) electron-phonon interaction strength, and α is an arbitrary constant. While α can be chosen arbitrarily, a natural choice is $\alpha = \langle n_\uparrow + n_\downarrow \rangle$ such that the Hartree term in the self-energy vanishes. We also note that in the anti-adiabatic limit ($\omega_0 \rightarrow \infty$ with $\lambda \equiv 2g^2/\omega_0$ fixed) the Holstein model becomes the attractive Hubbard model with the non-retarded interaction $-\lambda$. It is also useful to introduce the position and momentum operators for phonons,

$$X_i = (a_i^\dagger + a_i)/\sqrt{2}, \quad (2)$$

$$P_i = i(a_i^\dagger - a_i)/\sqrt{2}, \quad (3)$$

respectively.

Throughout the paper, we assume the absence of long-range order, and drive a system out of equilibrium via a quench of the electron-phonon coupling constant g at $t = 0_+$. To solve the problem, we employ the nonequilibrium DMFT.^{1,37} The DMFT formalism assumes a spatially local self-energy, and maps the lattice problem onto a quantum impurity model in a self-consistent manner. In order to describe the time evolution after a quench, one has to solve the DMFT equations on the L-shaped Kadanoff-Baym contour \mathcal{C} , which runs from $t = 0$ up to the maximum simulation time t_{max} along the real-time axis, back to $t = 0$, and then proceeds to $-i\beta$ along the imaginary-time axis, where $\beta = 1/T$ is the inverse temperature of the initial equilibrium state. We define the electron Green's function $G_{i,j,\sigma}(t, t')$ and the local

phonon Green's function $D(t, t')$ on this contour as

$$G_{i,j,\sigma}(t, t') = -i\langle T_{\mathcal{C}} c_{i,\sigma}(t) c_{j,\sigma}^\dagger(t') \rangle, \quad (4)$$

$$D(t, t') = -2i\langle T_{\mathcal{C}} X_i(t) X_i(t') \rangle, \quad (5)$$

where $T_{\mathcal{C}}$ is the contour-ordering operator. We denote the local electron Green's function by $G_{\text{loc}} \equiv G_{i,i,\sigma}$. Here, we omit the site index of G_{loc} and D , assuming a homogeneous state.

The effective impurity action for the Holstein model is

$$\begin{aligned} S_{\text{imp}} = & i \int_{\mathcal{C}} dt dt' \sum_{\sigma} d_{\sigma}^\dagger(t) \mathcal{G}_{0,\sigma}^{-1}(t, t') d_{\sigma}(t') \\ & + i \int_{\mathcal{C}} dt a^\dagger(t) (i\partial_t - \omega_0) a(t) \\ & - i \int_{\mathcal{C}} dt g(t) [a^\dagger(t) + a(t)] [n_{\uparrow}(t) + n_{\downarrow}(t) - \alpha], \quad (6) \end{aligned}$$

where the integrals run along the contour \mathcal{C} , d_{σ}^\dagger is the creation operator for electrons at the impurity site, and $\mathcal{G}_{0,\sigma}$ is the Weiss Green's function for the impurity problem, which is related to the hybridization function $\Delta_{\sigma}(t, t')$ by

$$\mathcal{G}_{0,\sigma}^{-1}(t, t') = (i\partial_t + \mu)\delta_{\mathcal{C}}(t, t') - \Delta_{\sigma}(t, t'), \quad (7)$$

where $\delta_{\mathcal{C}}$ is the delta-function on \mathcal{C} . We can simplify the form of the action by expressing a and a^\dagger with X and P and tracing out P . This yields

$$\begin{aligned} S'_{\text{imp}} = & i \int_{\mathcal{C}} dt dt' \sum_{\sigma} d_{\sigma}^\dagger(t) \mathcal{G}_{0,\sigma}^{-1}(t, t') d_{\sigma}(t') \\ & + i \int_{\mathcal{C}} dt dt' X(t) D_0^{-1}(t, t') X(t') \\ & - i\sqrt{2} \int_{\mathcal{C}} dt g(t) X(t) [n_{\uparrow}(t) + n_{\downarrow}(t) - \alpha], \quad (8) \end{aligned}$$

where

$$D_0^{-1}(t, t') = \frac{-\partial_t^2 - \omega_0^2}{2\omega_0} \delta_{\mathcal{C}}(t, t') \quad (9)$$

is the inverse of the bare phonon Green's function. In the solution of the DMFT equations, it is thus enough to consider the Green's function (5) for the phonons.

The Weiss Green's function \mathcal{G}_0 (or hybridization function Δ) is determined self-consistently in such a way that the electron Green's function for the impurity (G_{imp}) becomes identical to the local electron Green's function of the lattice (G_{loc}). In this paper, we consider the Bethe lattice with infinite coordination number ($z \rightarrow \infty$), where the self-consistency condition simplifies to^{1,27}

$$\Delta_{\sigma}(t, t') = v_*^2 G_{\text{loc},\sigma}(t, t') \quad (10)$$

with $v = v_*/\sqrt{z}$. In this case, the density of state is semi-elliptic,

$$D(\epsilon) = \frac{1}{2\pi v_*^2} \sqrt{4v_*^2 - \epsilon^2}, \quad (11)$$

and we set $v_* = 1$ in the following.

As can be seen in Eq. (8), the electrons interact with each other through the phonons and vice versa. To obtain the interacting Green's functions, we introduce the self-energies $\Sigma_{\sigma}(t, t')$ and $\Pi(t, t')$ for the electrons and phonons, respectively. These functions satisfy the Dyson equations

$$G_{\text{imp},\sigma}(t, t') = \mathcal{G}_{0,\sigma}(t, t') + [\mathcal{G}_{0,\sigma} * \Sigma_{\sigma} * G_{\text{imp},\sigma}](t, t'), \quad (12)$$

$$D(t, t') = D_0(t, t') + [D_0 * \Pi * D](t, t'), \quad (13)$$

where $*$ denotes a convolution on the contour \mathcal{C} .

The bare phonon Green's function can be expressed as

$$\begin{aligned} D_0(t, t') = & -i[\theta_{\mathcal{C}}(t, t') + f_B(\omega_0)] \exp\left(-i\omega_0 \int_{\mathcal{C}, t'}^t dt_1\right) \\ & - i[\theta_{\mathcal{C}}(t', t) + f_B(\omega_0)] \exp\left(-i\omega_0 \int_{\mathcal{C}, t}^{t'} dt_1\right), \quad (14) \end{aligned}$$

where $\theta_{\mathcal{C}}$ is the Heaviside function on \mathcal{C} , and $f_B(\omega_0) = (e^{\beta\omega_0} - 1)^{-1}$ is the Bose distribution function.

B. Properties of the phonon Green's function

We solve the nonequilibrium DMFT equations as described in Ref. 1, i.e., by solving a coupled set of integral-differential equations for the Matsubara (M), retarded (R), left-mixing (\neg) and lesser ($<$) components of the Green's functions (Appendix A). The advanced (A) and right-mixing (\neg) components can then be obtained by exploiting the Hermitian symmetry¹ or other special relations. Here, we explicitly state these relations, along with some other useful properties of the phonon Green's function $D(t, t')$. From Eq. (5), it follows that

$$D(t, t') = D(t', t), \quad (15)$$

and therefore

$$D^M(\tau, \tau') = D^M(\tau', \tau), \quad (16)$$

$$D^A(t', t) = D^R(t, t'), \quad (17)$$

$$D^{\neg}(\tau', t) = D^{\neg}(t, \tau'). \quad (18)$$

We also note that

$$D^{<}(t, t')^* = -D^{<}(t', t). \quad (19)$$

Furthermore, in contrast to G , the retarded part of D has no jump at $t = t'$, i.e.,

$$D^R(t + 0^+, t) = D^R(t, t + 0^+) = 0. \quad (20)$$

C. Observables

Kinetic energy— By comparing the Dyson equations for the lattice and for the effective impurity problem, we

obtain the expression for the electron kinetic energy,

$$\begin{aligned} E_{\text{kin}}(t) &\equiv \frac{-v}{N} \sum_{\langle i,j \rangle, \sigma} [\langle c_{i,\sigma}^\dagger(t) c_{j,\sigma}(t) \rangle + \text{h.c.}] \\ &= \frac{-i}{N} \sum_{i,\sigma} [\Delta_{i,\sigma} * G_{i,i,\sigma}]^<(t, t), \end{aligned} \quad (21)$$

where N is the number of lattice sites.

Electron-phonon correlation— By considering the equation of motion, $\partial_t c_{i,\sigma}(t) = i[\mathcal{H}(t), c_{i,\sigma}(t)]$, we obtain

$$\begin{aligned} i\partial_t G_{i,i,\sigma}(t, t')|_{t'=t+0_c^+} \\ = i \sum_j v_{i,j} \langle c_{i,\sigma}^\dagger(t) c_{j,\sigma}(t) \rangle - i\mu \langle c_{i,\sigma}^\dagger(t) c_{i,\sigma}(t) \rangle \\ + i\sqrt{2}g(t) \langle X(t) c_{i,\sigma}^\dagger(t) c_{i,\sigma}(t) \rangle, \end{aligned} \quad (22)$$

where $v_{i,j}$ is the hopping amplitude between sites i and j . We may now compare the expression (22) with the Dyson equation (12) for the impurity problem and use the expression (21) for the kinetic energy to obtain

$$i\sqrt{2}g(t) \langle X(t) c_{i,\sigma}^\dagger(t) c_{i,\sigma}(t) \rangle = [\Sigma_{i,\sigma} * G_{i,i,\sigma}]^<(t, t). \quad (23)$$

Phonon density— The density of phonons can be expressed in terms of the X and P operators as

$$\langle a^\dagger(t) a(t) \rangle = \frac{1}{2} [\langle X(t) X(t) \rangle + \langle P(t) P(t) \rangle] - \frac{1}{2}. \quad (24)$$

$\langle X(t) X(t) \rangle$ is obtained from $D(t, t)$, while $\langle P(t) P(t) \rangle$ is calculated from a second derivative of $D(t, t')$, as explained in the Appendix.

Total energy— The total energy per site is given by

$$\begin{aligned} E_{\text{tot}}(t) &= E_{\text{kin}}(t) - \mu \frac{1}{N} \sum_i \langle n_i \rangle + \frac{1}{N} \omega_0 \sum_i \langle a_i^\dagger(t) a_i(t) \rangle \\ &+ \frac{\sqrt{2}}{N} \sum_{i,\sigma} g(t) \left[\langle X_i(t) c_{i,\sigma}^\dagger(t) c_{i,\sigma}(t) \rangle - \alpha \langle X_i(t) \rangle \right]. \end{aligned} \quad (25)$$

D. Impurity Solvers

The effective impurity problem of the DMFT scheme is a non-trivial many-body problem. A numerically exact solution could in principle be obtained with the real-time quantum Monte Carlo (QMC) method, as for the Hubbard model.^{5,7} However, QMC suffers from a sign (phase) problem when implemented on the real axis, which will make it very difficult to reach the relatively long times required to simulate phonon dynamics. Therefore, we employ approximate diagrammatic impurity solvers (weak-coupling approximations) which we explain in the following.

1. *(Self-consistent) Migdal approximation*— The Feynman diagrams for the electron and phonon self-energies in the (self-consistent) Migdal approximation are shown

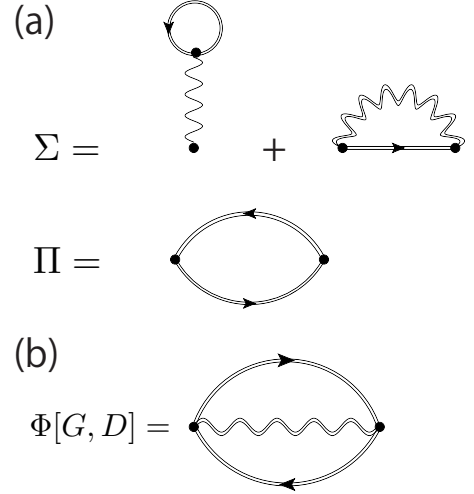


FIG. 2: (a) The electron self-energy (Σ) and phonon self-energy (Π) diagrams in the self-consistent Migdal approximation. Here, the tadpole diagram should be evaluated as $-iG_{\text{imp}}(t, t+0_c^+) - \alpha/2$. (b) The Luttinger-Ward functional Φ for the self-consistent Migdal approximation.

in Fig. 2(a). The corresponding formulas read

$$\begin{aligned} \Sigma(t, t') &= -\delta_c(t, t') g(t) \int_c dt_1 [\alpha + 2iG_{\text{imp}}(t_1, t_1+0_c^+)] D_0(t_1, t) g(t_1) \\ &+ iD(t, t') G_{\text{imp}}(t, t') g(t) g(t'), \end{aligned} \quad (26)$$

$$\Pi(t, t') = -i2g(t)g(t') G_{\text{imp}}(t, t') G_{\text{imp}}(t', t). \quad (27)$$

This approximation has been used to study the Holstein model in equilibrium, and its accuracy has been discussed in a number of papers.^{38,40–44} As long as g is not close to the critical value g_c for the transition to the bipolaronic insulating phase, it provides a qualitatively good description.^{38,43} Since the self-energies of the electrons and phonons involve dressed propagators (see sketch in Fig. 1(a)), we can take into account the interplay between the electrons and phonons in the dynamics. With the choice of $\alpha = \langle n_\uparrow + n_\downarrow \rangle$ in Eq. (1) the Hartree term vanishes, and we can define a Luttinger-Ward functional $\Phi[G, D]$ for this approximation as displayed in Fig. 2(b). Hence the Migdal approximation is a conserving one.

2. *Hartree-Fock approximation*— As we mentioned in the introduction, the Hartree-Fock (HF) approximation is also sometimes called the unrenormalized Migdal approximation.³⁹ In this approximation, the electron self-energy is given by

$$\begin{aligned} \Sigma(t, t') &= -\delta_c(t, t') g(t) \int_c dt_1 [\alpha + 2iG_{\text{imp}}(t_1, t_1+0_c^+)] D_0(t_1, t) g(t_1) \\ &+ iD_0(t, t') G_{\text{imp}}(t, t') g(t) g(t'). \end{aligned} \quad (28)$$

The Feynman diagrams for the self-energy have the same structure as in Fig. 2(a), but the dressed phonon propagator is replaced by the bare equilibrium propagator.

Thus, in the HF approximation, we ignore the phonon self-energy and there is no feedback from the electrons to the phonons (see Fig. 1(b)). Hence we cannot extract the dynamics for the phonons from this scheme. Also, the HF approximation cannot be derived from a Luttinger-Ward functional, and is thus not conserving.

The HF approximation has been used to study the equilibrium states³⁹ and nonequilibrium dynamics²⁶ of the Holstein model. For small g , the HF self-energy is expected to describe the effect of a bosonic heat bath on the electrons, and has been considered for this purpose in some DMFT studies.^{46,47} Also the results in Section III C will imply that the HF approximation cools the excited electrons down to the temperature of the (equilibrium) phonons.

III. RESULTS

In what follows, we focus on the case of $\omega_0 = 0.7$ and half-filling. We consider the weak coupling regime, i.e. systems with the coupling g smaller than the critical coupling g_c for the bipolaronic transition (CT-QMC calculations indicate that g_c is located at $0.8 \lesssim g_c \lesssim 0.85$ for $10 < \beta < 40$), but nevertheless with significant electron correlations. We have checked that our discussion and the results are also applicable to smaller phonon frequencies such as $\omega_0 = 0.4$.

A. Equilibrium

In this section, we benchmark the reliability of the Migdal and HF approximations as impurity solvers for DMFT, and clarify which properties are correctly captured by these methods. To this end, we consider equilibrium properties and first discuss the spectral functions computed with the two approximations. The spectral functions are defined by

$$\rho_{\text{ph}}(\omega) = -\text{Im}D^R(\omega)/\pi, \quad (29)$$

$$\rho_e(\omega) = -\text{Im}G_{\text{loc}}^R(\omega)/\pi \quad (30)$$

for phonons and electrons, respectively. We obtain these spectral functions by first computing the equilibrium propagators on the real-time axis and subsequently performing Fourier transformation.

In Fig. 3 (a)(c), we plot the phonon spectral functions $\rho_{\text{ph}}(\omega)$ calculated by the Migdal approximation at half filling with $\omega_0 = 0.7$ and indicated values of T and g . We find a single peak at $\omega = \omega_0^r$ (the renormalized phonon frequency), which shifts from $\omega = \omega_0$ (vertical lines) as the electron-phonon coupling g increases (phonon frequency renormalization). This result is consistent with previous $T = 0$ calculations based on the numerical renormalization group^{41,43} and the Migdal theory.⁴⁴ As the temperature is increased, the phonon frequency becomes less renormalized, indicating that the electron-phonon correlation becomes weaker at higher temperatures. The temperature dependence becomes more significant for larger g . In the HF approximation, on the other hand, $\rho_{\text{ph}}(\omega)$ has a delta function peak at $\omega = \pm\omega_0$

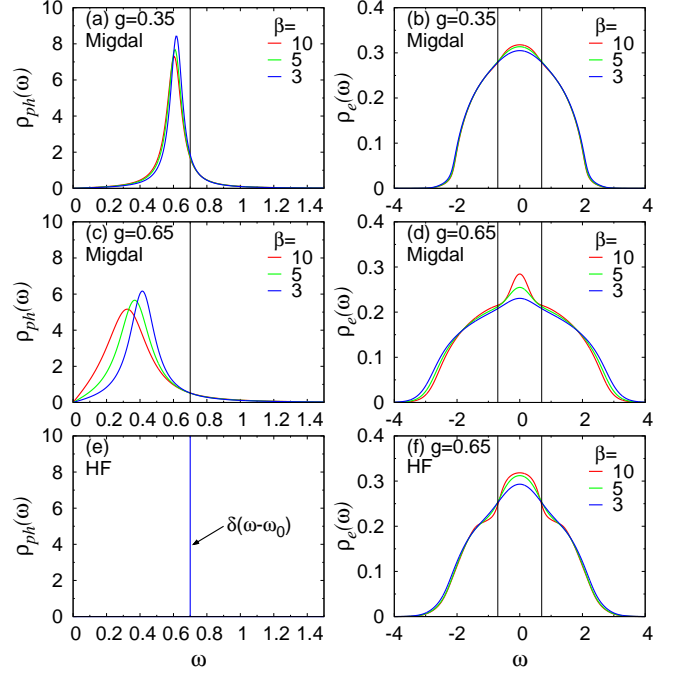


FIG. 3: (a)(c) The phonon spectral functions $\rho_{\text{ph}}(\omega)$ and (b)(d) the electron spectral functions $\rho_e(\omega)$ computed with the self-consistent Migdal approximation at half filling with $\omega_0 = 0.7$ for various values of g and T . (e)(f) are corresponding results in the HF approximation at half filling with $g = 0.65$. Vertical lines in each panel shows the bare phonon frequency $\omega = \pm\omega_0$.

[Fig. 3(d)], since the phonons are assumed to be noninteracting.

The electron spectral functions $\rho_e(\omega)$ are shown in Fig. 3(b)(d) for the Migdal approximation and in Fig. 3(f) for the HF approximation. In both cases, there emerges a peak in the spectrum at energies $|\omega| \lesssim \omega_0$ as the temperature is decreased. This peak represents quasiparticles (polarons) and becomes more pronounced as g increases. In the Migdal approximation, the peak becomes narrower with increasing g , which reflects the renormalization of the phonon frequency (ω_0^r), while in the HF approximation the width is fixed by the bare phonon frequency ω_0 .

In order to estimate the reliability of the Migdal and HF approximations, we show the corresponding self-energies on the Matsubara axis in Fig. 4. We compare them with the results computed using CT-QMC,⁴⁵ which, being exact within statistical errors, serve as a reference. It turns out that the HF approximation underestimates the self-energy, while the Migdal approximation slightly overestimates it. Clearly, the Migdal approximation is much closer to the CT-QMC results in the parameter regime considered here. The quantitative difference becomes clearer as the interaction g is increased. We conclude from these tests that the self-consistent Migdal approximation is more reliable and accurate than HF in a wide parameter regime, as long as we are not too close to the bipolaronic phase boundary. We therefore expect that the Migdal approximation also provides a better de-

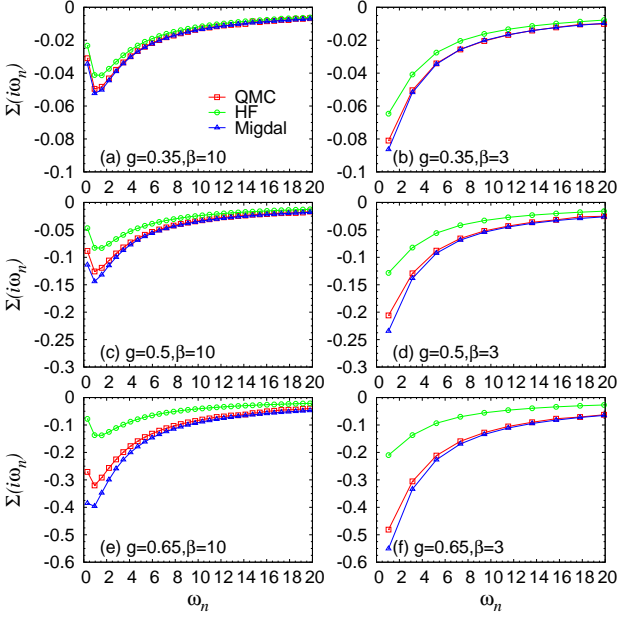


FIG. 4: The electron self-energies on the Matsubara axis calculated in DMFT with the Migdal, HF approximation, and CT-QMC impurity solvers for $\omega_0 = 0.7$ and indicated values of g and β .

scription of the nonequilibrium dynamics than the HF approximation.

B. Interaction quench: results of DMFT + Migdal approximation

In this section, we study the time evolution of the Holstein model after an interaction quench of the electron-phonon coupling $g = g_i \rightarrow g_f$ at $t = 0_+$ using the self-consistent Migdal approximation as an impurity solver. The system is initially noninteracting ($g_i = 0$) at equilibrium with temperature $T = 0$. Although the length of the imaginary branch of the contour \mathcal{C} is infinite in this case ($\beta = \infty$), we can still treat the noninteracting initial state numerically, since the R and $<$ components are decoupled from the imaginary branch of the contour in the Dyson equations due to $\Sigma^M, \Sigma^<, \Pi^M, \Pi^< = 0$. Similar quench problems have been studied for the Hubbard model with DMFT+QMC.^{5,7} With this initial condition, the momentum distribution $n(\epsilon_k, t) = -iG_k^<(t, t)$ exhibits a discontinuous jump at $\epsilon = 0$ (i.e., the Fermi surface) for short times, while it is expected to become a smooth function when the system is finally thermalized at nonzero temperature. The height of the jump $\Delta n(t)$ is thus a useful quantity that allows one to keep track of the thermalization process and measure how much $n(\epsilon, t)$ deviates from the thermal distribution. In the following, we compare the relaxation behavior of local observables to that of $n(\epsilon, t)$.

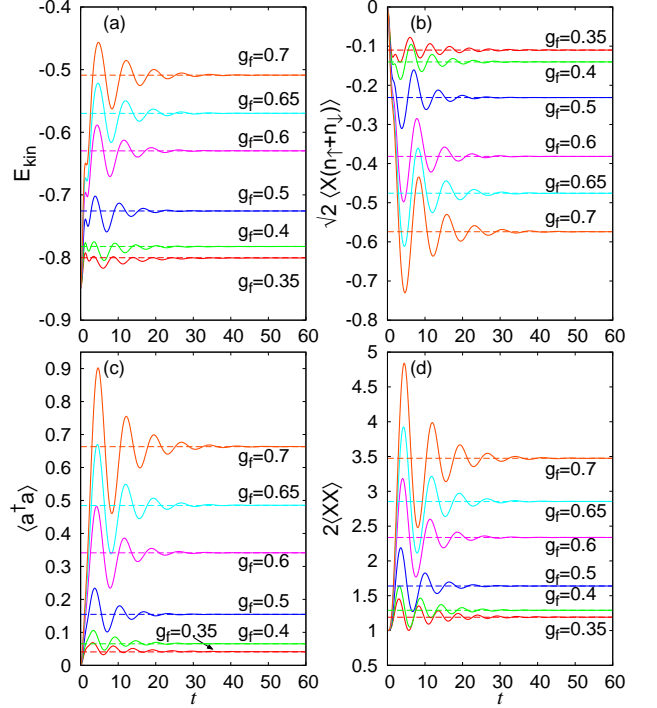


FIG. 5: Temporal evolution of the local quantities after an interaction quench from $g = 0$ and $T = 0$ with $\omega_0 = 0.7$: (a) E_{kin} , (b) $\sqrt{2}\langle X(n_\uparrow + n_\downarrow) \rangle$, (c) $\langle a^\dagger a \rangle$, and (d) $2\langle XX \rangle$. Dashed lines in each panel indicate the expected thermal values for each value of g_f .

1. Local observables

In Fig. 5, we show the time evolution of the kinetic energy, the correlation between the phonon displacement and the density of electrons $\sqrt{2}\langle X(n_\uparrow + n_\downarrow) \rangle$, the phonon density $\langle a^\dagger a \rangle$, and the variance of the phonon displacement $2\langle XX \rangle$. All these local observables show coherent oscillations with a certain frequency, which becomes slower as we increase g_f . It turns out that this frequency is twice the renormalized phonon frequency, $2\omega_0^r$. This observation can be explained as follows. First, let us suppose that each local phonon oscillates as $X(t) \sim \cos(\omega_0^r t)$. Since the interaction quench does not select the direction of lattice distortion (either $X > 0$ or $X < 0$), the statistical distribution for the lattice displacement, $F(X, t)$, is roughly an even function of X and oscillates with π/ω_0^r . The former is in fact exactly true in our case, since there is a particle-hole symmetry ($c \leftrightarrow c^\dagger, X \leftrightarrow -X$). This naturally explains the oscillation of $2\langle XX \rangle$ with frequency $2\omega_0^r$. Provided that the phonon dynamics affects the electronic states through $F(X)$, it is natural to expect oscillations of the other quantities with frequency $2\omega_0^r$.

As time increases, the oscillations are damped and the amplitude of the oscillations becomes very small after $t = 60$ in all the cases shown here. An important question is whether the steady value at $t \gtrsim 60$ corresponds to the thermal value which should be reached in the long-time limit. We can examine this by looking at the total

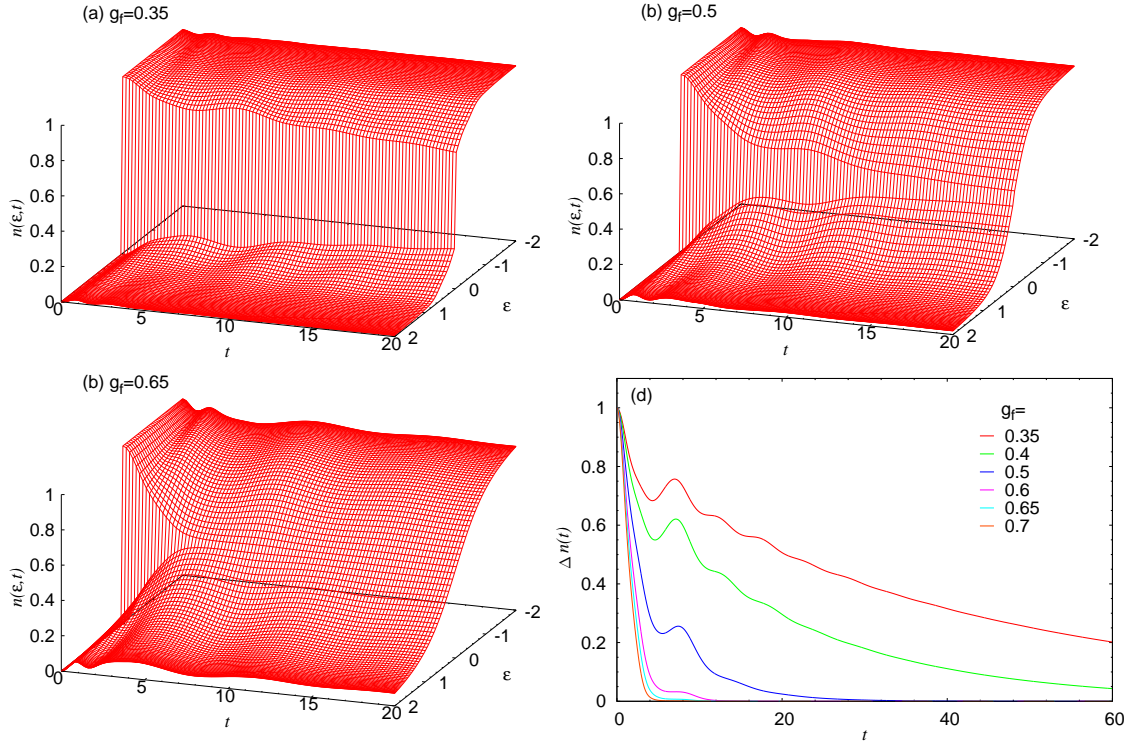


FIG. 6: (a)-(c) Temporal evolution of the momentum distribution for $\omega_0 = 0.7$ after quenches to various g_f . (d) Temporal evolution of $\Delta n(t)$ for various values of g_f and $\omega_0 = 0.7$.

energy. After the quench the total energy is conserved, since the Hamiltonian is time-independent. Therefore, we can define a temperature T_{th} through the relation

$$E_{\text{tot}}(t > 0) = \frac{\text{Tr} e^{-\mathcal{H}_f/T_{\text{th}}} \mathcal{H}_f}{\text{Tr} e^{-\mathcal{H}_f/T_{\text{th}}}}, \quad (31)$$

where \mathcal{H}_f is the Hamiltonian after the quench. If the system thermalizes, expectation values of observables should approach those of the equilibrium state with the corresponding temperature T_{th} . For example, the thermal kinetic energy is given by

$$E_{\text{kin,th}} = \frac{-v}{N} \sum_{\langle i,j \rangle, \sigma} \frac{\text{Tr} e^{-\mathcal{H}_f/T_{\text{th}}} (c_{i,\sigma}^\dagger c_{j,\sigma} + \text{h.c.})}{\text{Tr} e^{-\mathcal{H}_f/T_{\text{th}}}}. \quad (32)$$

The dashed lines in Fig. 5 indicate the estimated thermal values at T_{th} for each observable. We can see that the steady state values indeed approach the thermal values. However, we have to note that this does not necessarily mean that the system is fully thermalized, as we will discuss in the next section.

2. Momentum distribution function

In order to examine whether the system is really close to a thermalized state once the oscillations in the above local quantities are damped, let us look at the evolution

of the momentum distribution for electrons $n(\epsilon_k, t) = -iG_k^<(t, t)$ [Fig. 6(a)-(c)] and its jump $\Delta n(t)$ at $\epsilon = 0$ [Fig. 6(d)]. We start from $T = 0$, $g = 0$, so that $\Delta n(0) = 1$. The jump does not immediately disappear after the quench, but decreases gradually. As we increase the interaction, $\Delta n(t)$ vanishes faster, as in the case of the Hubbard model.^{5,7} The main qualitative difference is that $\Delta n(t)$ oscillates in the present case of the Holstein model.

Now we are in a position to focus on the relation between the dynamics of $\Delta n(t)$ and that of the local observables. A key finding is that we may distinguish two qualitatively different types of relaxation behavior in the Holstein model, depending on the interaction strength within the parameter regime explored here. The first type of relaxation dynamics is observed in the interaction regime $g_f \lesssim 0.5$. At $g_f = 0.35$, for instance, the phonon oscillation is damped and the local (momentum integrated) quantities are essentially thermalized at $t = 60$ (Fig. 5), while momentum-resolved quantities of electrons exemplified by $\Delta n(t)$ are not [Fig. 6(d)], i.e., $n(\epsilon, t)$ is far from being close to the thermal distribution. While the height of the jump does not exhibit a plateau-like structure, as is seen in the infinite dimensional Hubbard model,^{5,7} this may still be regarded as a prethermalization phenomenon in the sense that *local (momentum integrated) quantities thermalize fast, while momentum dependent quantities, such as $n(\epsilon, t)$, remain clearly nonthermal*. As a result, the longer-time relaxation process is bottlenecked and dominated by electrons. This key observation charac-

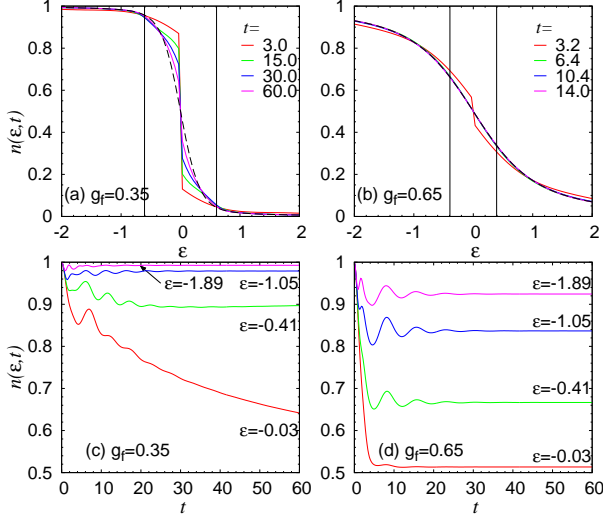


FIG. 7: (a)(b) Momentum distribution function at fixed t for $g_f = 0.35$ (a) and 0.65 (b). For (b) we chose special times, t , at which $E_{\text{kin}}(\tilde{t}) = E_{\text{kin},\text{th}}$. The dashed lines in (a)(b) show the momentum distribution in equilibrium at T_{th} , but it is invisible in (b) due to an almost perfect overlap with the data for $t \geq 6.4$. Vertical lines show $\epsilon = \pm\omega_0^r$. (c)(d) Time evolution of $n(\epsilon, t)$ for several values of ϵ with $g_f = 0.35$ (c) and 0.65 (d).

terizes the behavior of the Holstein model in the weak-coupling regime.

In Fig. 7(a)(c), we take a closer look at the relaxation of the momentum distribution $n(\epsilon, t)$ for $g_f = 0.35$. Figure 7(a) shows $n(\epsilon, t)$ with fixed t , while Fig. 7(c) shows the evolution of $n(\epsilon, t)$ with fixed ϵ . The relaxation time strongly depends on the energy ϵ : When $\epsilon \gtrsim \omega_0^r$ the relaxation is fast, while for $\epsilon \lesssim \omega_0^r$ the relaxation is slow, see Fig. 7(a). This behavior is similar to the HF results discussed in Ref. 25.

The second type of relaxation behavior appears for $g_f \gtrsim 0.5$. At $g_f = 0.65$, for example, $\Delta n(t)$ vanishes [Fig. 6(b)] before the oscillations of the momentum-integrated observables become negligible (Fig. 5). Once these oscillations are fully damped, $n(\epsilon, t)$ also becomes identical to the thermal value. We have to note that the disappearance of the jump in $\Delta n(t)$ by no means implies that the distribution $n(\epsilon, t)$ is thermal. Rather, the distribution continues to oscillate away from the Fermi energy as shown in Fig. 7(d), while $\Delta n(t)$ becomes very small before $t = 8$ [Fig. 6(d)]. Damping of oscillations is related to the lifetime of phonons as will be further discussed in the relation with the self-energy of phonons. Hence phonons govern the long-time behavior in this case. Interestingly, however, we can see in Fig. 7(b) that $n(\epsilon, \tilde{t})$ becomes indistinguishable from the thermalized distribution (dashed line, which almost perfectly coincides with the plotted distributions) at those times \tilde{t} at which $E_{\text{kin}}(\tilde{t}) = E_{\text{kin},\text{th}}$ [Eq. (32)] holds.

The change from the first (electron-dominated) to second (phonon-dominated) type of thermalization is a “crossover”, i.e., the change is smooth and there is no sudden transition in the characteristics of the thermal-

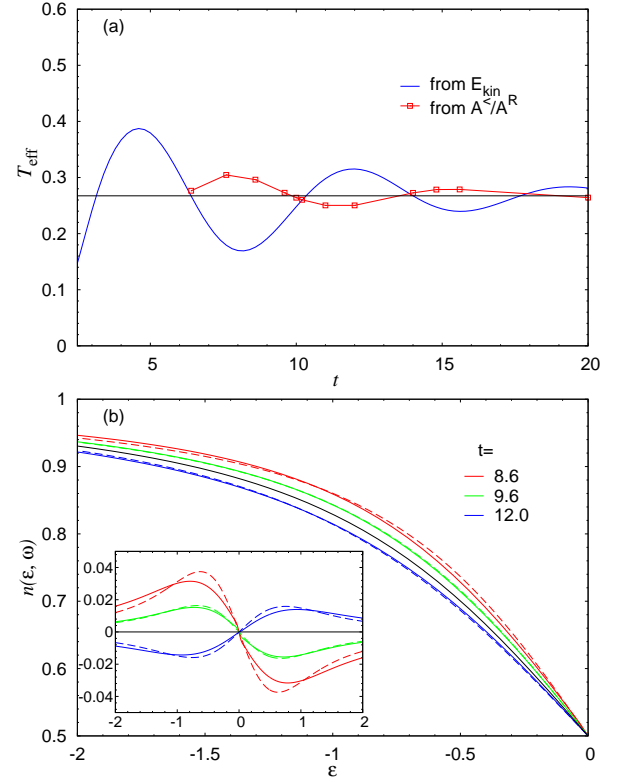


FIG. 8: (a) Temporal evolution of the effective temperature defined in Eq. (33) (blue curve) and from the slope of the “nonequilibrium distribution function” (red curve with squares) for $g_f = 0.65$ and $\omega_0 = 0.7$. The horizontal line is T_{th} . (b) The momentum distribution at $t = 8.6, 9.6$ and 12.0 for the same parameters (solid curves) as compared with the equilibrium distribution functions (dashed lines) for the corresponding T_{eff} defined in Eq. (33). The inset shows the difference from the equilibrium distribution at T_{th} (black curve in the main panel).

ization process (thermalization crossover). The crossover between these two types occurs around $g_f \sim 0.5$, where the oscillations and $\Delta n(t)$ vanish on a similar time scale.

At this point we can discuss the relation between the present result and the phenomenological two-temperature model.¹⁸ We note that our situation is rather different from what is assumed in the two-temperature model. In the latter, the assumption made is that the electron degrees of freedom thermalize fast because of the Coulomb interaction, while in our case we only consider the electron-phonon coupling. Still, it is worthwhile to discuss the relation between the two models. In the first type of relaxation ($g_f \lesssim 0.5$) in the Holstein model, the relaxation time strongly depends on ϵ , and it would not be proper to describe it by a single decay rate as in the two-temperature model. More importantly, it is difficult to define a meaningful effective temperature for the electrons in this case, since the relaxations of $n(\epsilon, t)$ occur on different time scales for different ϵ .

In the second type of relaxation ($g_f \gtrsim 0.5$), on the

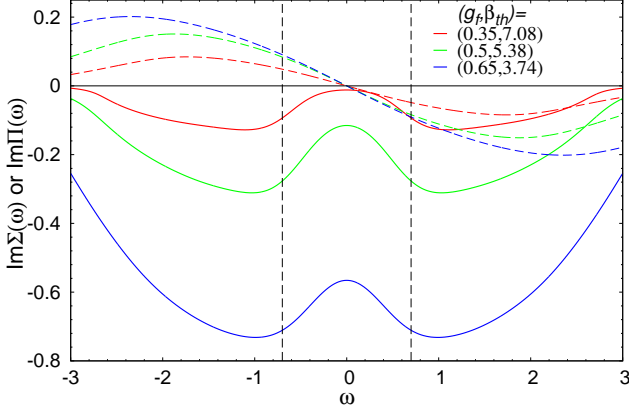


FIG. 9: Imaginary part of the electron self-energy (solid lines) and phonon self-energy (dashed lines) at equilibrium with T_{th} for various values of g_f . The vertical lines show $\omega = \pm\omega_0$.

other hand, the dynamics of the momentum distribution can be reasonably explained by defining a time-dependent “effective temperature” $T_{\text{eff}}(t)$ via the relation

$$E_{\text{kin,th}}(T_{\text{eff}}(t), g_f, \omega_0) = E_{\text{kin}}(t, g_f, \omega_0). \quad (33)$$

The time evolution of the effective temperature T_{eff} is shown by the blue curve in Fig. 8(a). Figure 8(b) plots the momentum distribution at three representative times $t = 8.6, 9.6, 12.0$. One can see that at these times, $n(\epsilon, t)$ is different from the equilibrium distribution at T_{th} . However, $n(\epsilon, t)$ is rather well reproduced by the equilibrium distribution $n(\epsilon)$ for g_f and $T_{\text{eff}}(t)$ (see inset). In this sense, $T_{\text{eff}}(t)$ defined in Eq. (33) is a meaningful effective temperature, which allows to predict momentum dependent electronic properties.

3. Damping rates and self-energies

In this section, we show that the different relaxation rates of physical quantities ($E_{\text{kin}}, \Delta n(t) \dots$) can be related to the g -dependence of the electron (Σ) and phonon (Π) self-energies. In Fig. 9, we plot the imaginary part of the electron self-energy and the phonon self-energy at equilibrium with $T = T_{\text{th}}$. When we look at the electron self-energy, we can see that $\text{Im}\Sigma$ is relatively small in the energy range $|\omega| < |\omega_0^r|$, which becomes even more evident at lower temperatures. This is consistent with the picture that electron (hole)-like quasiparticles cannot emit (absorb) phonons in this energy window, since the states below (above) the Fermi level are occupied (empty) at low enough temperatures. As a result, the quasiparticles survive for long time in this energy range, since, roughly speaking, $-2\text{Im}\Sigma(\omega = \epsilon)$ can be regarded as the relaxation rate. We note that this picture also qualitatively explains the different relaxation time scales of $n(\epsilon, t)$ for different ϵ , illustrated in Fig. 7(a)(c).

Now let us consider the lifetime of electron quasiparticles in more detail. In the small ω regime, the system, if it is a Fermi liquid, has an electron self-energy of the

form

$$\Sigma^R(\omega) = (1 - 1/Z)\omega - i\Gamma + O(\omega^2), \quad (34)$$

where Z is the quasiparticle residue and $\Gamma \propto T^2$. For $g_f = 0.35$ there are some deviations from this behavior ($\Gamma \propto T^2$), but the imaginary part is still small. It then follows that quasiparticles with momentum \mathbf{k} have a renormalized energy $\epsilon_{\mathbf{k}}^r \equiv Z\epsilon_{\mathbf{k}}$ and a lifetime of $(2Z\Gamma)^{-1}$ in the low-energy regime.

We can extract the lifetime of phonons from the phonon self-energy in a similar manner. For small enough ω , the phonon self-energy can be expanded as

$$\Pi^R(\omega) = A - iB\frac{\omega}{\omega_0} + C\frac{\omega^2}{\omega_0^2} + O(\omega^3), \quad (35)$$

and the dressed Green’s function becomes

$$D^R(\omega) \simeq \frac{2Z'\omega_0}{(\omega - \omega'_0 + iZ'B)(\omega + \omega'_0 + iZ'B) + Z'^2B^2}, \quad (36)$$

where $\omega'_0 = Z'\omega_0(1 + A/\omega_0)^{1/2}$ and $Z' = (1 - 2C/\omega_0)^{-1}$. Here, we note that ω'_0 is an approximation of the renormalized frequency ω_0^r . One can neglect the second term (Z'^2B^2) in the denominator of $D^R(\omega)$ (36) if $B \ll \omega'_0$, since the absolute value of the first term in the denominator is at least of $O(B\omega'_0)$, which is much larger than the second term of $O(B^2)$. It thus follows that $D^R(t)$ decays with a damping rate $Z'B$. We have checked this prediction and found that $Z'B$ indeed explains the damping of $D^R(t)$ in the interaction regime considered. Hence the lifetime of phonons can be identified with $(2Z'B)^{-1}$.

Now we come to the key result of the present work. In Figure 10(a) we plot the decay rates for electrons ($2Z\Gamma$) and phonons ($2Z'B$), extracted from the self-energies, against g_f . Around $g_f = 0.5$ these two quantities cross each other, so that $2Z\Gamma < 2Z'B$ for $g_f < 0.5$, while $2Z\Gamma > 2Z'B$ for $g_f > 0.5$. This means that as long as the quasiparticle picture is valid, the electrons (in the low-energy regime) decay more slowly than the phonons for $g_f < 0.5$, while the phonons decay more slowly than the electrons for $g_f > 0.5$. Indeed, these coefficients turn out to provide a good description for the relaxation process after a quench in the Holstein model.

In Fig. 10(a), we also show the electron decay rate of $\Delta n(t)$ obtained by exponential curve fitting as shown in Fig. 10(b). Here we use data from $t = 0$ up to $t = 60$ or up to $\Delta n(t) = e^{-10}$. The decay rate increases as g_f increases, and to a good approximation matches the value of $2Z\Gamma$. In the small- g_f regime the difference is very small, while $2Z\Gamma$ tends to overestimate the exponent of $\Delta n(t)$ in larger- g_f regime. On the other hand, the phonon decay rate $2Z'B$ shows up in the damping of $E_{\text{kin}}, \langle Xn \rangle, \langle XX \rangle$ and $\langle a^\dagger a \rangle$. As an example, we have fitted the envelopes of the oscillations of $\langle XX \rangle - \langle XX \rangle_{\text{th}}$ with an exponential, Fig. 10(c), and plot the corresponding decay rates in Fig. 10(a). We note that the amplitude oscillations for other quantities ($E_{\text{kin}}, \langle Xn \rangle$ and $\langle a^\dagger a \rangle$) decay at almost the same rate. As can be seen in Fig. 10(a), it turns out that $2Z'B$ provides a good explanation for the decay rates of local

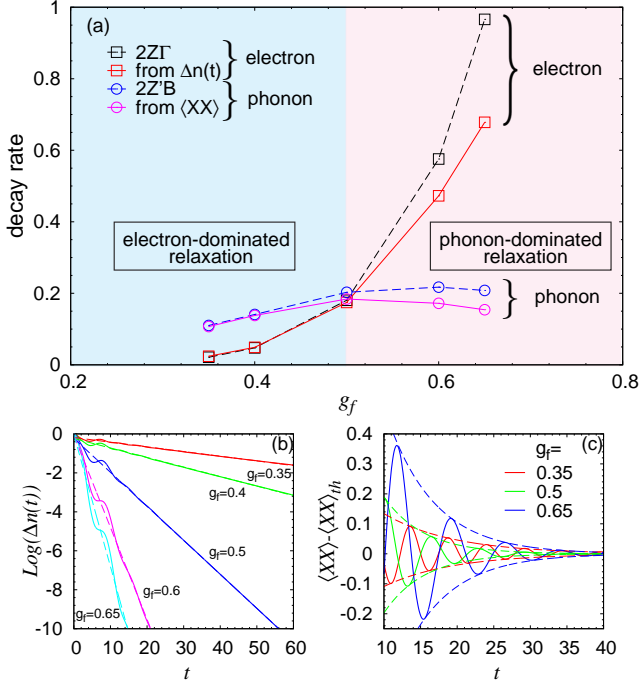


FIG. 10: (a) Plot of different energy scales (inverse relaxation times) against g_f . (b) Log plot of $\Delta n(t)$ for various g_f . The results of exponential fits are shown as dashed lines. (c) Damping of the amplitude of the oscillation of $\langle XX \rangle - \langle XX \rangle_{th}$. The envelopes obtained from exponential fits are shown with dashed curves.

quantities. To be more precise, while the agreement with $2Z'B$ is very good at $g_f \lesssim 0.5$, the damping rate predicted by the phonon self-energy tends to overestimate the damping rate of the $\langle XX \rangle - \langle XX \rangle_{th}$ oscillations and this tendency becomes clearer as we increase g_f .

The above analysis enables us to identify the origin of the two different relaxation behaviors as a different coupling dependence of the decay rates of the electrons and phonons. In the weaker coupling regime, the decay time for phonons is shorter than for electrons. Hence the phonon oscillations are damped before $n(\epsilon, t)$ thermalizes (electron-dominated thermalization). The fact that the values of local observables after the relaxation of the phonons are already very close to the thermal values is, however, nontrivial. In the second type of relaxation (the stronger coupling regime), it follows from the self-energy analysis that the relaxation time for the electrons is shorter than that for the phonons (Fig. 10(a)). Hence $\Delta n(t)$ vanishes and the momentum distribution approaches its thermal value quickly. However, since the phonons are still relaxing and oscillating, the electrons are forced to move with them (phonon-dominated thermalization).

4. Spectral functions

We next discuss how the two different types of relaxation manifest themselves in the spectral function and

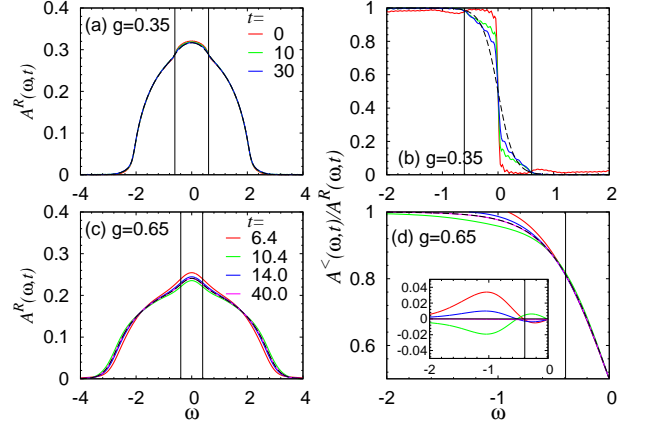


FIG. 11: (a)(c) Nonequilibrium spectral function $A^R(\omega, t)$ at different t for $g_f = 0.35$ and 0.65 respectively. (b)(d) Nonequilibrium distribution function at different t for $g_f = 0.35$ and 0.65 respectively. The dashed curves show the thermal A^R and distribution functions. Vertical lines in each panel show ω_0^r at equilibrium at T_{th} for each g_f . The inset in (d) shows the deviation of the distribution function from the thermal one.

nonequilibrium distribution function. In nonequilibrium, we define the electron spectral function A^R and occupied spectral function $A^<$ as

$$A^{R,<}(\omega, t) = \mp \frac{1}{\pi} \text{Im} \int_t^\infty d\bar{t} e^{i\omega(\bar{t}-t)} G_{loc}^{R,<}(\bar{t}, t), \quad (37)$$

where $-$ is for R and $+$ is for $<$. For a slowly varying state, $A^<(\omega, t)$ corresponds to the time-resolved photoemission spectrum and A^R to the time-resolved total spectral function. From these one can define the “nonequilibrium distribution function” $A^<(\omega, t)/A^R(\omega, t)$. In Fig. 11, we show $A^R(\omega, t)$ and $A^<(\omega, t)/A^R(\omega, t)$ at different times. The results for $g_f = 0.35$ are shown in panels (a) and (b). We note that even at $t = 0$, A^R shows a peak structure around $\omega = 0$ and therefore is different from the spectral function of the free system. This is because $A^R(\omega, t)$ includes information on later times than t . The “nonequilibrium distribution function” $A^</A^R$ in the energy interval $|\omega| > |\omega_0^r|$ relaxes to the thermal value quickly, while for $|\omega| < |\omega_0^r|$, the relaxation is slow. This is consistent with the behavior of the momentum distribution and with a previous analysis of the photoexcited Holstein model.²⁶ Here we note that small wiggles in Fig. 11 (b) are Fourier cutoff artifacts.

The dynamics for a larger $g_f = 0.65$ is shown in panels (c) and (d). Here we again choose the special times at which $E_{kin} = E_{kin,th}$. As can be seen, the effective temperature defined in Eq. (33) becomes less helpful to explain the behavior of the spectral function and the distribution function: The nonequilibrium spectral function A^R still changes with time, while the nonequilibrium distribution function $A^</A^R$ cannot be fitted over the whole energy range with an equilibrium distribution function. This failure is not too surprising, since the effective temperature was determined by instantaneous temporal in-

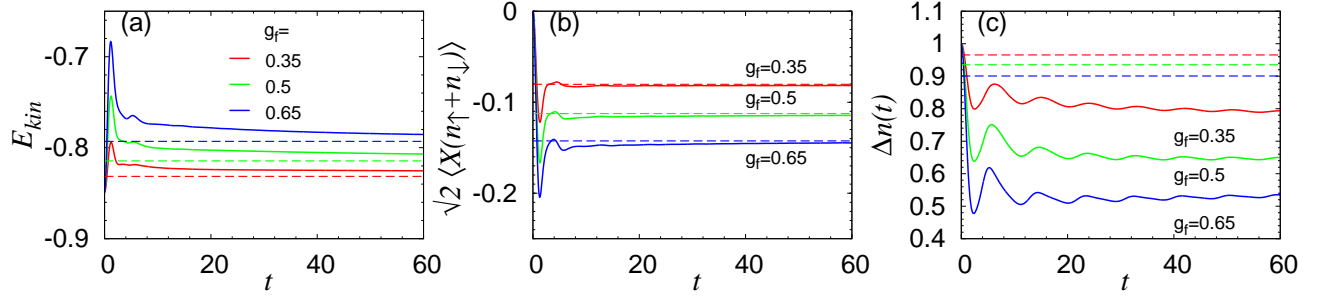


FIG. 12: Temporal evolution of (a) the kinetic energy, (b) $\sqrt{2}\langle X(n_{\uparrow} + n_{\downarrow}) \rangle$, and (c) $\Delta n(t)$ after quenches to the indicated values of g , calculated with the HF approximation ($\omega_0 = 0.7$). Horizontal lines indicate the thermal values at $T = 0$.

formation, while $A^<$ and A^R includes information on future times. In Fig. 8 (a), we show the effective temperature determined from the slope of $A^</math>/ A^R at $\omega = 0$. Even though this effective temperature oscillates around T_{th} in the opposite way from the T_{eff} determined from E_{kin} , both estimates agree well with each other at the special points where $E_{\text{kin}} = E_{\text{kin,th}}$.$

The time dependent spectra and distribution functions oscillate with time and eventually (for $t \gtrsim 40$), relax to the thermal A^R and Fermi distribution function, see Fig. 11(c)(d). As is evident in Fig. 8 (a) and Fig. 11(d), the difference to the relaxation in the weak-coupling regime ($g_f = 0.35$) is that not only the energy range $|\omega| < |\omega_0^r|$, but also $|\omega| > |\omega_0^r|$ exhibits a clear time dependence in the time range considered.

C. Interaction quench: results of DMFT + Hartree-Fock approximation

Now we can compare the above results from the self-consistent Migdal scheme with the Hartree-Fock result for the interaction quench from $T = 0$, $g = 0$ to $g_f \neq 0$. As we discussed in Section IID, in this approximation the phonons are described by the noninteracting equilibrium propagator, so that the physical quantities that we can study are E_{kin} , $\langle X(n_{\uparrow} + n_{\downarrow}) \rangle$, and $n(\epsilon, t)$. In Fig. 12, we show the results for $\omega_0 = 0.7$ and several values of g_f . One striking difference from the self-consistent Migdal results is that the oscillations are damped very quickly, with vanishing oscillations for $t > 10$. While the relaxation is slow, these momentum-integrated quantities seem to approach a steady value in the long-time limit. However, since the total energy is not conserved, it does not make sense to define an expected temperature of the thermal state as in the Migdal approximation. In fact, as was discussed in Ref. 46, the HF type self-energy for electrons is expected to act as a heat bath which cools the system down to the temperature of the initial equilibrium state (i.e. the temperature of the bare phonon propagator), which is $T = 0$ here. In Fig. 12, we plot as horizontal lines the equilibrium value at $T = 0$ obtained by extrapolation from nonzero temperatures. Even though there remains a significant difference in E_{kin} even at $t = 60$, it appears that both E_{kin} and $\langle X(n_{\uparrow} + n_{\downarrow}) \rangle$ gradually relax to the thermal values at $T = 0$.

Next, we look at the dynamics of $\Delta n(t)$ and $n(\epsilon, t)$.

The long-time dynamics of $\Delta n(t)$ is shown in Fig. 12(c) up to $t = 60$. In all the cases, the jump height $\Delta n(t)$ becomes smaller than unity, but remains large and exhibits slowly damped oscillations. For larger g_f the jump height decreases further, but we could not find a fast decay of the jump as in the Migdal approximation, up to $\lambda = 3$ which is already well beyond the coupling regime in which the HF approximation can be trusted. (The QMC calculations indicate that the critical coupling for the bipolaronic transition, g_c , is located at $0.8 \lesssim g_c \lesssim 0.85$ for $10 < \beta < 40$.) Another difference from the Migdal approximation is that the frequency of the oscillation is the bare phonon frequency $\omega_0 = 0.7$. In the discussion below, we will show that this qualitative difference can be solved by adding the lowest-order diagram for the dressed phonons. The fact that the jump $\Delta n(t)$ does not vanish is consistent with the expectation that the phonons in HF effectively act as a heat bath and that the electrons are thus cooled down to $T = 0$. Furthermore, the fact that at $t = 60$, $\Delta n(t)$ is still far from the expected value for $T = 0$ shows that the cooling rate is very low. This can be understood as follows: In the $T = 0$ equilibrium state, $\text{Im}\Sigma(\omega) \propto \omega^2$ for a Fermi liquid. Hence, the decay rate for $\Delta n(t)$ is expected to approach 0, as the system approaches the thermalized state.

Now, let us take a closer look at the momentum distribution function. Figure 13 shows the dynamics of $n(\epsilon, t)$ in more detail. For both $g = 0.35$ and $g = 0.65$, the distribution at large $|\epsilon|$ relaxes fast to the equilibrium value at $T = 0$, while the distribution for small $|\epsilon|$ relaxes slowly. This aspect is consistent with the prediction of the Migdal approximation and the previous simulations of a pump excited Holstein model,²⁴ and also with the structure of the self-energy. However, strictly speaking, we find that the energy window exhibiting a slow relaxation in $n(\epsilon, t)$ is larger than the window $-\omega_0 < \epsilon < \omega_0$ predicted by the self-energy analysis. This is probably due to the fact that after the quench, many quasiparticles are excited in the energy range $-\omega_0 < \epsilon < \omega_0$, so that quasiparticles (assuming this notion is well defined) with energy $|\epsilon| > |\omega_0|$ can decay less easily. In addition to this, one finds that $n(\epsilon, t)$ shows more pronounced oscillations than in the Migdal approximation, and that each $n(\epsilon, t)$ has a different frequency, see Fig. 13(b)(d). These oscillations with different frequencies lead to the complicated structure of $n(\epsilon, t)$ shown in Fig. 13(a)(c). We can thus attribute the fast damping of the oscillations in E_{kin} to the dephasing of the momentum distribution, which is

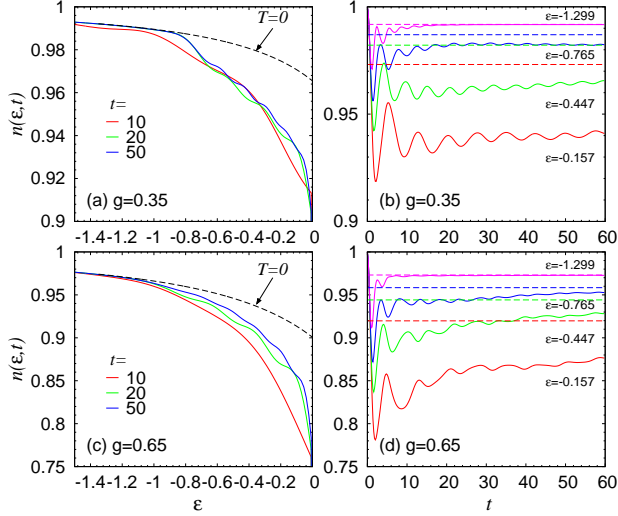


FIG. 13: Evolution of $n(\epsilon, t)$ after the quench calculated within the HF approximation ($\omega_0 = 0.7$). Dashed horizontal lines indicate the thermal values at $T = 0$.

a different scenario from the damping in the Migdal approximation, where the oscillations of the electrons are tied to the dynamics of the phonons and both are damped simultaneously.

To sum up, all of these results are consistent with the system approaching the $T = 0$ state and we thus conclude that the HF approximation is not appropriate for describing the dynamics of the isolated Holstein model.

D. Discussion

We are interested here in the relaxation and thermalization processes of an isolated electron-phonon system. As can be seen from the comparison to the equilibrium results from CT-QMC (Fig. 4), the self-consistent Migdal approximation is much more accurate than HF in a wide parameter regime. Hence it is natural to expect that the Migdal approximation is the better approximation in the nonequilibrium case as well. When we compare the dynamics after an interaction quench, both approximations describe a thermalization of the system. However, the type of thermalization is very different. In the self-consistent Migdal approximation, the system relaxes to the state whose temperature is determined by the total energy after the quench, which is in general different from the initial temperature. On the other hand, in the HF approximation, the system approaches the (interacting) state with the phonon temperature (T_{ph}), which is equal to the initial temperature, and hence the phonon degrees of freedom act as a heat bath. We note that, even though the relaxation is very slow in the $T_{\text{ph}} = 0$ case discussed in the previous section, if one starts from nonzero temperatures, the system approaches to the equilibrium state at $T_{\text{ph}} > 0$ is much faster (not shown).

The behavior of the HF approximation is artificial if we consider the time evolution of an isolated system, and hence the Migdal approximation should provide a more reliable description of the dynamics of the isolated Hol-

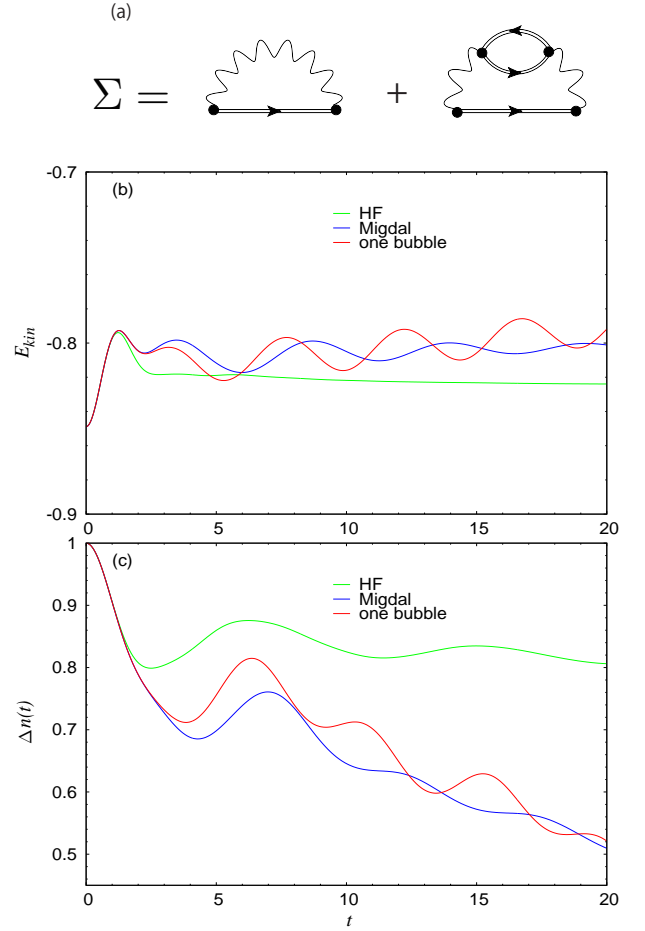


FIG. 14: (a) Self-energy of the one-bubble approximation. (b) Comparison of the three approximations for the evolution of E_{kin} at $\omega_0 = 0.7$ after a quench from $g_i = 0, T = 0$ to $g_f = 0.35$. (c) Comparison of the evolution of $\Delta n(t)$ at $\omega_0 = 0.7$ after a quench from $g_i = 0, T = 0$ to $g_f = 0.35$.

stein model. On the other hand, we note that it may be possible to use the HF approximation as a phenomenological model for electrons coupled to a heat bath, as in Refs. 46,47. The latter studies were for the Hubbard model, with an electron-electron interaction U , and the coupling g to the phonon bath was assumed to be small, so that the only relevant effect of the phonons was to provide a dissipation channel. However, if one wants to study dynamical aspects of the phonons and the feedback of the nonequilibrium phonons on the electrons, as in our case, the HF approximation is not sufficient. This point should be taken into account in studies related to real materials, such as high- T_c cuprates, with significant electron-phonon coupling, where phonons are expected to play, in the relaxation dynamics, a role more intrinsically than a heat bath. To be more precise, since real materials are not isolated systems but open systems, energy dissipation from the excited region should be taken into account in a realistic description. Then the timescale on which these dissipative processes become relevant depends on the details of the material and the experimental set-up.

So far, we have revealed that the dynamics in the Migdal approximation and that in the HF approximation are totally different. Hence one may wonder which particular self-energy diagrams cause this difference. To address this question, we considered the self-energy shown in Fig. 14(a), where we added to the HF approximation the next-order diagram for the phonon propagator (we omitted the Hartree term in the figure, which is zero here), and we call this approximation the “one-bubble approximation”. Including this bubble makes the dynamics very different from that predicted by the HF approximation. Some results are shown in Fig. 14(b)(c), where we consider a quench from $T = 0, g = 0$. All the three approximations behave similarly for short time, but the one-bubble approximation gives results which are qualitatively more similar to the dynamics in the Migdal approximation than to the HF approximation. Furthermore, the one-bubble approximation already reproduces characteristic behavior of the Migdal approximation. For example, the momentum-summed quantities (Fig. 14(b)) and $\Delta n(t)$ (Fig. 14(c)) oscillate with a frequency of about $2\omega_0$. Thus, even the simplest correction to the phonon propagator yields a significantly different time evolution. This implies that it is crucial to consider the dynamics of the phonons when one investigates the time evolution of isolated electron-phonon systems.

IV. CONCLUSIONS

In this paper, we have studied the dynamics of the Holstein model after a quench (sudden switch-on) of the interaction using the nonequilibrium DMFT. As an impurity solver, we employed the self-consistent Migdal approximation, which includes the dynamics of phonons via the phonon self-energy. In all the cases, it turns out that the local (momentum-summed) quantities show essentially $2\omega_0^r$ oscillations (with ω_0^r the renormalized phonon frequency), as is expected for responses involving phonon oscillations. Furthermore, we revealed that there exists a thermalization crossover between two distinct regimes: The first regime, corresponding to $g \lesssim 0.5$, shows a fast damping of the oscillations originating from the phonon dynamics, with the momentum-summed quantities approaching the thermal values quickly, while the momentum distribution of electrons exhibits a much slower relaxation (electron-dominated relaxation). The second regime corresponds to stronger couplings ($g \gtrsim 0.5$). Here, the jump in the momentum distribution quickly vanishes, and the momentum distribution approaches its thermal value. However, since the phonon damps more slowly, the momentum distribution oscillates with the phonon around the thermal value (phonon-dominated relaxation). We then showed that we can define an instantaneous effective temperature from the electron kinetic energy, which can reasonably describe the dynamics of the full momentum distribution of the electrons. We have discussed that changes in the relaxation behavior can be related to changes in the values of the electron and phonon self-energies, which cross as the electron-phonon coupling is increased.

We also discussed the importance of the phonon dynamics by analyzing and comparing the results obtained from the HF approximation, which does not include the

phonon dynamics. It turns out that the latter approximation predicts a totally different type of relaxation process and effectively act as a heat bath. We also discussed that the dynamics of the Migdal approximation is already qualitatively recovered by adding the simplest “one bubble” correction to the phonon propagator.

Our work can serve as a benchmark for further studies of electron-phonon systems. In particular, it will be interesting to understand the dynamics of ordered phases in electron-phonon systems,^{48,49} a topic that will be discussed in a separate publication.

Acknowledgments

The authors would like to thank D. Golez and A. Millis for fruitful discussions. YM, NT, and HA wish to thank the Fribourg University for hospitality when the manuscript was written. YM, NT and HA have been supported by LEMSUPER (EU-Japan Superconductor Project) from JST, and YM is supported by JSPS Research Fellowships for Young Scientists and Advanced Leading Graduate Course for Photon Science (ALPS). NT was supported by Grant-in-Aid for Scientific Research (Grant Nos. 25104709, 25800192). PW acknowledges support from FP7/ERC starting Grant No. 278023.

V. APPENDIX

A. Dyson equation

To investigate the dynamics of a certain type of Green’s function $\Theta(t, t')$, one needs to solve the Dyson equation, which can be expressed in the form

$$[1 - F] * \Theta = Q. \quad (38)$$

If we explicitly write down this equation for the retarded, lesser and \neg components, it becomes

$$\Theta^R(t, t') - \int_{t'}^t d\bar{t} F^R(t, \bar{t}) \Theta^R(\bar{t}, t') = Q^R(t, t') \quad (39)$$

$$\begin{aligned} \Theta^<(t, t') - \int_0^t d\bar{t} F^R(t, \bar{t}) \Theta^<(\bar{t}, t') &= Q^<(t, t') \\ &+ \int_0^{t'} d\bar{t} F^<(t, \bar{t}) \Theta^A(\bar{t}, t') - i \int_0^\beta d\bar{\tau} F^\neg(t, \bar{\tau}) \Theta^\neg(\bar{\tau}, t') \end{aligned} \quad (40)$$

$$\begin{aligned} \Theta^\neg(t, \tau') - \int_0^t d\bar{t} F^R(t, \bar{t}) \Theta^\neg(\bar{t}, \tau') &= Q^\neg(t, \tau') \\ &+ \int_0^\beta d\bar{\tau} F^\neg(t, \bar{\tau}) \Theta^M(\bar{\tau}, \tau'). \end{aligned} \quad (41)$$

When Θ corresponds to G or D , the components Θ^A and Θ^\neg are related to Θ^R and Θ^\neg (although the relation is different for the fermionic and bosonic Green’s function), so the above set of equations is closed, and we only need to solve these three equations.

B. Derivatives of the phonon propagator

Here we discuss the properties of the derivative of the phonon Green's function. With Eq. (1),

$$i\partial_t X(t) = \omega_0(-a^\dagger(t) + a(t))/\sqrt{2}, \quad (42)$$

so we find

$$\begin{aligned} D_{d1}(t, t') &\equiv \frac{\partial_t D(t, t')}{\omega_0} \\ &= -i2\langle T_c P(t) X(t') \rangle, \end{aligned} \quad (43)$$

where $P = \frac{-a^\dagger + a}{i\sqrt{2}}$ and $[X, P] = i$. In the same manner,

$$\begin{aligned} D_{d2}(t, t') &\equiv \frac{\partial_{t'} D(t, t')}{\omega_0} \\ &= -i2\langle T_c X(t) P(t') \rangle. \end{aligned}$$

In addition, we calculate the second derivative of D ,

$$\begin{aligned} D_{d1,d2}(t, t') &\equiv \frac{\partial_t \partial_{t'} D(t, t')}{\omega_0^2} \\ &= \frac{2}{\omega_0} \delta_c(t, t') - i2\langle T_c P(t) P(t') \rangle. \end{aligned} \quad (44)$$

If we know D, D_{d1}, D_{d2} and $D_{d1,d2}$ we can recover the usual boson Green's function defined as $-i\langle T_c a(t) a^\dagger(t') \rangle$, and, in particular, the phonon density $\langle a^\dagger(t) a(t) \rangle$, Eq. (24). These quantities can be evaluated with D and Π by considering the following equations,

$$D_{d1}(t, t') = D_{0,d1}(t, t') + [D_{0,d1} * \Pi * D](t, t'), \quad (45)$$

$$D_{d2}(t, t') = D_{0,d2}(t, t') + [D * \Pi * D_{0,d2}](t, t'), \quad (46)$$

$$D_{d1,d2}(t, t') = D_{0,d1,d2}(t, t') + [D_{0,d1} * \Pi * D_{d2}](t, t'). \quad (47)$$

Since

$$D_{d1}^R(t, t') = D_{d2}^A(t', t), \quad (48)$$

$$D_{d1}^<(t, t') = -D_{d2}^<(t', t)^*, \quad (49)$$

$$D_{d1}^\neg(t, \tau') = D_{d2}^\neg(\tau', t), \quad (50)$$

we can focus on the R , $<$ and \neg components for Eq. (45), (46) and (47). In particular, to evaluate the phonon density $\langle a^\dagger a \rangle$, we only need to know $D_{d1,d2}^<$. In this case we only need to evaluate Eq. (45) and solve the $<$ part of Eq. (47).

-
- ¹ H. Aoki, N. Tsuji, M. Eckstein, M. Kollar, T. Oka, and P. Werner, *Rev. Mod. Phys.* **86**, 779 (2014).
 - ² S. R. Manmana, S. Wessel, R. M. Noack, and A. Muramatsu, *Phys. Rev. Lett.* **98**, 210405 (2007).
 - ³ C. Kollath, A. M. Läuchli, and E. Altman, *Phys. Rev. Lett.* **98**, 180601 (2007).
 - ⁴ M. Moeckel and S. Kehrein, *Phys. Rev. Lett.* **100**, 175702 (2008).
 - ⁵ M. Eckstein, M. Kollar and P. Werner, *Phys. Rev. Lett.* **103**, 056403 (2009).
 - ⁶ P. Barmettler, M. Punk, V. Gritsev, E. Demler, and E. Altman, *Phys. Rev. Lett.* **102**, 130603 (2009).
 - ⁷ M. Eckstein, M. Kollar and P. Werner, *Phys. Rev. B* **81**, 115131 (2010).
 - ⁸ N. Tsuji, M. Eckstein, and P. Werner, *Phys. Rev. Lett.* **110**, 136404 (2013).
 - ⁹ N. Tsuji and P. Werner, *Phys. Rev. B* **88**, 165115 (2013).
 - ¹⁰ H. U. R. Strand, M. Eckstein and P. Werner, *arXiv:1405.6941*.
 - ¹¹ S. Iwai, M. Ono, A. Maeda, H. Matsuzaki, H. Kishida, H. Okamoto, and Y. Tokura, *Phys. Rev. Lett.* **91**, 057401 (2003).
 - ¹² L. Perfetti, P. A. Loukakos, M. Lisowski, U. Bovensiepen, H. Berger, S. Biermann, P. S. Cornaglia, A. Georges, and M. Wolf, *Phys. Rev. Lett.* **97**, 067402 (2006).
 - ¹³ H. Okamoto, H. Matsuzaki, T. Wakabayashi, Y. Takahashi, and T. Hasegawa, *Phys. Rev. Lett.* **98**, 037401 (2007).
 - ¹⁴ H. Okamoto, T. Miyagoe, K. Kobayashi, H. Uemura, H. Nishioka, H. Matsuzaki, A. Sawa, and Y. Tokura, *Phys. Rev. B* **83**, 125102 (2011).
 - ¹⁵ D. Fausti, R. I. Tobey, N. Dean, S. Kaiser, A. Dienst, M. C. Hoffmann, S. Pyon, T. Takayama, H. Takagi, and A. Cavalleri, *Science* **331**, 189 (2011).
 - ¹⁶ L. Stojchevska, I. Vaskivskyi, T. Mertelj, P. Kusar, D. Svetin, S. Brazovskii, D. Mihailovic, *Science* **344**, 177 (2014).
 - ¹⁷ S. L. Johnson, P. Beaud, E. Vorobeve, C. J. Milne, E. D. Murray, S. Fahy, and G. Ingold, *Phys. Rev. Lett.* **102**, 175503 (2009).
 - ¹⁸ P. B. Allen, *Phys. Rev. Lett.* **59**, 1460 (1987).
 - ¹⁹ L. Vidmar, J. Bonca, M. Mierzejewski, P. Prelovsek, and S. A. Trugman, *Phys. Rev. B* **83**, 134301 (2011).
 - ²⁰ D. Golez, J. Bonca, L. Vidmar, and S. A. Trugman, *Phys. Rev. Lett.* **109**, 236402 (2012).
 - ²¹ D. Golez, J. Bonca, and L. Vidmar, *Phys. Rev. B* **85**, 144304 (2012).
 - ²² K. Yonemitsu and N. Maeshima, *Phys. Rev. B* **79**, 125118 (2009).
 - ²³ G. De Filippis, V. Cataudella, E.A. Nowadnick, T.P. Devereaux, A.S. Mishchenko, and N. Nagaosa, *Phys. Rev. Lett.* **109**, 176402 (2012).
 - ²⁴ M. Sentef, et al, *Phys. Rev. X* **3**, 041033 (2013).
 - ²⁵ A. F. Kemper, et al, *Phys. Rev. B* **87**, 235139 (2013).
 - ²⁶ A. F. Kemper *et al.*, *arXiv:1403.5245*.
 - ²⁷ W. Metzner and D. Vollhardt, *Phys. Rev. Lett.* **62**, 324 (1989); A. Georges and G. Kotliar, *Phys. Rev. B* **45**, 6479 (1992); A. Georges, G. Kotliar, W. Krauth, and M. J. Rozenberg, *Rev. Mod. Phys.* **68**, 13 (1996).
 - ²⁸ P. Werner and M. Eckstein, *Phys. Rev. B* **88**, 165108 (2013).
 - ²⁹ P. Werner and M. Eckstein, *arXiv:1403.7376*.
 - ³⁰ J. Berges, S. Borányi, and C. Wetterich, *Phys. Rev. Lett.* **93**, 142002 (2004).
 - ³¹ M. Schiró and M. Fabrizio, *Phys. Rev. Lett.* **105**, 076401 (2010).
 - ³² M. Schiró and M. Fabrizio, *Phys. Rev. B* **83**, 165105 (2011).

- ³³ E. Pazy and A. Vardi, Phys. Rev. A **72**, 033609 (2005).
- ³⁴ F. Herrera and R. V. Krems, Phys. Rev. A **84**, 051401 (2011).
- ³⁵ J. P. Hauge and C. MacCormick, New J. Phys. **14**, 033019 (2012).
- ³⁶ M. Hohenadler, Phys. Rev. B **88**, 064303 (2013).
- ³⁷ J.K. Freericks, V.M. Turkowski, and V. Zlatić, Phys. Rev. Lett. **97**, 266408 (2006).
- ³⁸ J. Bauer, J. E. Han and O. Gunnarsson, Phys. Rev. B. **84**, 184531 (2011).
- ³⁹ J. K. Freericks, M. Jarrell and D. J. Scalapino, Phys. Rev. B. **48**, 6302 (1993).
- ⁴⁰ J. K. Freericks, Phys. Rev. B. **50**, 403 (1994).
- ⁴¹ D. Meyer, A. C. Hewson and R. Bulla, Phys. Rev. Lett, **89**, 196401 (2002).
- ⁴² M. Capone and S. Ciuchi, Phys. Rev. Lett. **91**, 186405 (2003).
- ⁴³ W. Koller, D. Meyer and A. C. Hewson, Phys. Rev. B, **70**, 155103 (2004).
- ⁴⁴ J. P. Hauge, N. d' Ambrumenil, J Low Temp Phys, **151**, 1149 (2008).
- ⁴⁵ P. Werner and A. J. Millis, Phys. Rev. Lett. **99**, 146404 (2007).
- ⁴⁶ M. Eckstein and P. Werner, Phys. Rev. Lett. **110**, 126401 (2013).
- ⁴⁷ M. Eckstein and P. Werner, Journal of Physics: Conf. Series **427**, 012005 (2013).
- ⁴⁸ Y. Murakami, P. Werner, N. Tsuji and H. Aoki, Phys. Rev. B **88**, 125126 (2013).
- ⁴⁹ Y. Murakami, P. Werner, N. Tsuji and H. Aoki, arXiv:1402.6456 (2014).